Article

Highly Defective Dark Nano Titanium Dioxide: Preparation via Pulsed Laser Ablation and Application

Elena D. Fakhrutdinova[1], Anastasiia V. Shabalina[1]*, Marina A. Gerasimova[2],
Anna L. Nemoykina[3], Olga V. Vodyankina[4], Valery A. Svetlichnyi[1]*

[1] Laboratory of Advanced Materials and Technology, Tomsk State University, Tomsk 634050, Russia:
    fakhrutdinovaed@gmail.com (E.D.F.); shabalinaav@gmail.com (A.V.S.); v_svetlichnyi@bk.ru (V.A.S.)

[2] Laboratory of Biophotonics, Siberian Federal University, Krasnoyarsk 660041, Russia; marina_2506@mail.ru
    (M.A.G.)

[3] Laboratory of Biopolymers and Biotechnology, Tomsk State University, Tomsk 634050, Russia;
    nemoykina@rambler.ru (A.L.N.)

[4] Laboratory of Catalytic Research, Tomsk State University, Tomsk 634050, Russia; vodyankina_o@mail.ru
    (V.O.V.)

* Correspondence: shabalinaav@gmail.com; Tel.: +7-3822-531-591 (A.V.S.)

Abstract: Dark titania powder was obtained via pulsed laser ablation (Nd:YAG laser, 1064 nm, 7 ns) in water and subsequent air drying. It was then undergone the thermal treatment to study the changes occurring in the material. The structure, composition, and properties of the obtained powders were studied using TEM, BET, XRD, DSC, XPS, Raman and UV-vis spectroscopy, and PL methods. The processes taking place in the initial material under heating were studied. The electronic structure of the semiconductor materials was investigated and the nature of the defects providing the visible light absorption was revealed. The photocatalytic and antibacterial activities of the materials obtained were also studied. It was found that dark titania obtained via LAL exhibited catalytic activity in the phenol photodegradation process under visible light (> 420 nm) and showed antibacterial activity against *S. aureus* and bacteriostatic effect towards *E. coli.*

1. Introduction

Titania TiO_2 is a multifunctional semiconducting material that has found application in a wide variety of fields [1, 2]. TiO_2 has three crystal modifications: anatase, rutile, and brookite [3]. Also different non-stoichiometric titanium oxide phases are possible to form. Magneli phases of Ti_nO_{2n-1} [4] are of a great interest among them. Depending on their structure, titanium oxides exhibit significantly different properties. So, rutile is an inert oxide, and is used in cosmetics, food industry, paints and varnishes, etc. [5]. Anatase is active, and it is known as an effective photocatalyst [6, 7]. Different titania forms are widely used in biomedicine [8, 9].

Normally, titanium dioxide is a white powder with the band gap energy of 3.0-3.2 eV, and it does not absorb the light in the visible range [3]. This limits its use in photocatalysis. To increase the effectiveness and to widen the spectral range of TiO_2 activity in photocatalysis, doping [10-12], core@shell structures formation [13], decoration [14], and complex composite/hybrid oxides creation [15, 16] are used.

Nowadays, "dark" titania is also of a great interest. To change the color of the initially white oxide is possible, for example, via its reducing. So, in the work [17], polycrystalline titanium dioxide

45   in a reducing media changes its color from white to yellow, then to brown and it becomes blue-black
46   in the end. Black color is due to the presence of the oxygen vacancies of different types, Ti^{3+} and Ti^{4+}
47   interstitial ions, and Ti-H bond [18]. Thus, the disorder of the titanium dioxide lattice plays a
48   significant role in the formation of black TiO_2. Structural defects lead to the appearance of additional
49   energy levels in the band gap, which is a key factor for the optical and catalytic activity of materials.
50   Dark titanium dioxide was first obtained in 2011 by heating of white TiO_2 at 200°C and a hydrogen
51   pressure of 20.0 bar [19]. To date, there are several dozen of works devoted to the obtaining and
52   study of black titanium dioxide, including reviews [20-22]. The main methods for the synthesis of
53   black titanium dioxide are hydrogenation of white titanium dioxide at high and low pressure [21,
54   22], treatment with hydrogen plasma [23], electrochemical and chemical reduction [23, 24], and laser
55   irradiation [20, 25]. Of great interest is the synthesis of dark oxide from a titanium metal target by
56   pulsed laser ablation in a liquid (LAL).
57   The high-energy nonequilibrium LAL method is currently widely used to obtain a wide range
58   of nanoparticles [26–29] and for surface structuring [30, 31]. LAL also allows one to get colloids of
59   dark titanium oxide. To date, several tens of works have been devoted to the ablation of metallic
60   titanium, for example [32–45]. Despite this, studies of titanium LAL and the resulting nanostructures
61   continue to attract the great interest. This is due to the wide variability of the method depending on
62   the radiation characteristics, other parameters of the ablation process, and the composition of the
63   solution. It is reported that by the means of varying the radiation characteristics, the reaction
64   medium, and other experimental parameters, particles of various sizes, stoichiometrics, defects'
65   content, and crystal structures can be obtained from a metal target. Even under rather similar
66   experimental conditions, it is possible to obtain titanium dioxide nanoparticles with various
67   properties. So, only at ns LAL of Ti in water by the radiation of the fundamental harmonic of a
68   Nd:YAG laser (1064 nm) with varying experimental parameters, the crystal structure (amorphous,
69   anatase, brookite, rutile) changes, and particles with various defects, non-stoichiometric composition
70   are obtained [32-36]. The use of shorter pulses (pico-sec, femto-sec) and wavelengths, further
71   diversifies the size, morphology, and structure of the NPs obtained [37, 38]. An important role in the
72   result is played by the processes of secondary interaction. This is confirmed by experiments on
73   additional laser irradiation of colloids [39, 40]. In addition, the properties of powders obtained by
74   drying colloids synthesized by LAL have almost not been studied.
75   The aim of this work was to study the morphology, structure, and optical properties of
76   nanopowders obtained by drying and further heat treatment of dark titanium oxide colloids
77   synthesized by LAL of metal titanium in water. As well as testing the photocatalytic and
78   antibacterial properties of the obtained powders.

79   **2. Materials and Methods**

80   *2.1. Synthesis of the materials*

81   Nanocrystalline TiO_2 powders were synthesized in two stages. At the first stage, the colloidal
82   solution was prepared by the method of pulsed laser ablation of bulk target in water. On the next
83   stage, the colloidal solution was dried.
84   Basic harmonic of the Nd:YAG laser (LOTIS TII, model LS2131M-20) was used for the LAL. The
85   wavelength of 1064 nm and pulse energy up to 180 mJ were used. Pulse duration and pulse
86   frequency were 7 ns and 20 Hz, respectively. Ablation in the cylindrical 100 ml glass vessel
87   continued for 3 h. It was performed in distilled water without using any precursors or additional
88   stabilizing agents. Stirring of the solution during ablation was ensured by natural convection. Laser
89   radiation was focused through the sidewall of the vessel using a short-focus lens F=50 mm. The
90   distance between the target and the inner side of the vessel wall was of 4 mm. The wavelength and
91   the focusing conditions were selected to minimize the light scattering and secondary excitation of
92   particles in the colloidal solution. The radiated power density on the target surface decreased with
93   time because of absorption and scattering in the colloid. So, the power of radiation was being
94   increased to compensate for this energy fall.

95   Metal Ti plate (99.9%) with a size of 10×25×1 mm was used as a target. In order to ensure the
96   uniform irradiation and to prevent the craters' formation on the target surface, it was automatically
97   moved in the XY plane orthogonal to the laser beam by two linear stepper motor translation stages
98   (Standa, model 8MT173-50). The concentration of particles in the dispersion was controlled on the
99   basis of target mass loss.
100   To obtain a powder, the colloid was dried in the air in an open glass vessel at the temperature
101   up to 60°C. Then 3 g of nanocrystalline powder were obtained. Several portions of the sample were
102   annealed in the muffle chamber at temperatures in the range 200-1000°C. The materials obtained
103   were marked as TiO_2_ini, 200, 400, 600, 800, 1000, respectively.

2.2. Characterization of the materials

105   Transmission electron microscopy (TEM) was applied to study the microstructure of the
106   materials. The images and selected area electron diffraction patterns were obtained using
107   microscope HT-7700, Hitachi (Japan). Drops of freshly prepared dispersions were placed onto
108   copper grids coated with carbon film and then dried at room temperature. Scanning electron
109   microscopic study was carried out on Vega 3H, Tescan (Czech Republic).
110   Specific surface area (S_{BET}) and pore size distribution were determined from the data obtained
111   on gas adsorption analyzer of specific surface and porosity TriStar II 3020, Micromeritics (USA).
112   Previous to the measurements the samples were degassed under vacuum (10^{-2} Torr) at 200°C for 2 h
113   (TiO_2_ini sample was degassed at room temperature). Pore size distribution and porosity were
114   calculated from the desorption isotherms by BJH method (Barrett-Joyner-Halenda).
115   The X-ray diffraction (XRD) method was used to study the phase composition and average
116   regions of coherent scattering of the powder samples. Shimadzu XRD 6000 (Japan) diffractometer
117   was used to record the diffraction patterns. The phase compositions were identified using the PDF-4
118   database. The phases content was calculated using PowderCell 2.4 software complex.
119   Thermal analysis in the region of 25-1000°C was performed using Netzsch STA 449 F3 Jupiter®
120   (Germany) with the rate of 10 grad/min under dry air flow with the rate of 50 ml/min. The samples
121   were placed in alundum (Al_2O_3) crucibles.
122   Raman spectra were recorded using the Raman microscope InVia, Renishaw (United
123   Kingdom), with laser excitation at wavelength of 785 nm in the range of 100-1000 cm^{-1} at power < 1
124   mW to prevent the phase changes in the samples under the analysis conditions.
125   X-ray photoelectron spectroscopy (XPS) data was obtained using X-ray photoelectron
126   spectrometers KRATOS ES 300, Kratos Analytical (United Kingdom) with a MgKα source. Before
127   loading into the spectrometer, the samples were deposited onto a conductive carbon tape. In order to
128   assess the qualitative composition of the surface and identify the presence of impurities, the survey
129   spectra were obtained in the range of 0-1150 eV with the energy step of 1 eV at analyzer pass energy
130   HV=50 eV. The quantitative composition of the surface and the charge states of the elements were
131   determined by obtaining precision spectra of individual photoelectron lines with 0.1 eV step at
132   analyzer pass energy HV=25 eV.
133   UV-Vis absorption spectra of nanocrystalline powders were examined by the method of diffuse
134   reflectance spectroscopy (DRS) on Cary 100SCAN, Varian (Australia) spectrophotometer with an
135   accessory DRA-CA-30I, Labsphere (USA) in the wavelength range of 230-800 nm. MgO was used as
136   a measurement standard. The band gap was calculated from diffuse reflection spectra using the
137   Tauc method for indirect semiconductors [46]. Photoluminescence (PL) spectra of the samples were
138   recorded at room temperature on a Fluorolog 3-22 spectrometer, Horiba, Jobin Yvon (USA) with the
139   different excitation wavelengths form the region of 320-750 nm.

2.3. Photocatalytic and antibacterial activity study

141   The photocatalytic activity of the materials was assessed on the base of phenol degradation by
142   the visible light. Metal-halogenic lamp Master Colour CDM-TD 70W/942, Philips (Germany) with
143   the cut-off filter YG11 (410 nm) (Fig. S1) was used. A portion of 50 mg of the powder under study
144   was dispersed in 50 ml of phenol solution in water ($5×10^{-5}$ M). Before photocatalytic experiment, the

145 dark stage was performed for 1 h to rich the sorption equilibrium. After that the irradiation was
146 carried out for 1 h at the constant stirring by a magnet stirrer. The luminosity on the surface of the
147 solution was 66 klx (direct sunlight is characterized with 30-120 klx).

148   Photodegradation and sorption values were calculated by the phenol concentration decrease.
149 The concentration was determined photometrically (spectrophotometer Cary 100SCAN) by the
150 decrease of the optical density of the solution at the long-wave band of absorption. The particles
151 were removed from the solution via ultracentrifugation by centrifuge Allegra 64R, Beckman Coulter
152 (USA).

153   The antibacterial activity of the prepared inorganic-organic composites as model wound
154 dressing materials was tested in accordance with the standard ISO 20743:2013 [47] and by using two
155 bacteria strains: gram-positive *Staphylococcus aureus* (*S. aureus*, test strain ATCC 25923) and
156 gram-negative *Escherichia coli* (*E. coli*, test strain B-6954, Russian Collection of Microorganisms). The
157 experimental conditions and the procedure of the antibacterial activity measurement are described
158 in details in our previous work [48]. The NPs from the initial colloid of dark titania were precipitated
159 onto a cotton fabric "TexLine" ("Textilnaya Liniya", Ivanovo, Russia, density 120 g/cm^2). The values
160 of antibacterial activity A were determined using Formula (1):

$$A = (lgC_t - lgC_0) - (lgT_t - lgT_0) = F - G, \qquad (1)$$

161 where $F = (lgC_t - lgC_0)$ is the growth rate on the control (TiO$_2$-free) cotton sample; lgC_t is the average
162 decimal logarithm of the number of bacteria found on three control samples incubated for 24 h; lgC_0
163 the average decimal logarithm of the number of bacteria observed on three control samples
164 immediately upon seeding with bacteria; $G = (lgT_t - lgT_0)$ the growth rate on the sample loaded with
165 antibacterial NPs; lgT_t the average value of decimal logarithm of the number of bacteria observed
166 after incubation for 24 h on three treated samples; and lgT_0 the average decimal logarithm of bacteria
167 number observed immediately after bacteria seeding on three cotton samples loaded with TiO$_2$.

168 **3. Results and Discussion**

169 *3.1. Structure study*

170 3.1.1. Microscopic data

171   The initial sample was obtained via LAL and air drying. Then, it was annealed at different
172 temperatures in the region of 200-1000°C. Before thermal treatment, the powder is dark. After 200
173 and 400°C the color changes to light-grey, at 600°C it becomes white, and after heating up to 800 or
174 1000°C the sample is light-yellow. To reveal the structure change of the material during thermal
175 treatment, a microscopic study was applied.

176   TEM images of the materials obtained via LAL and subsequent thermal treatment are presented
177 in Figure 1. The as-prepared sample is represented with small spherical particles around 5-10 nm,
178 and larger particles of 80 nm. Such a bimodal size distribution is quite characteristic of the NPs
179 obtained via LAL [41, 44]. This is due to the specific features of the particles' formation mechanism
180 under non-equilibrium conditions when the laser beam interacts with the solid target in the liquid
181 media [28].

182   Thermal treatment led to the size and shape of the particles change. The size increased due to
183 sintering. Spheres coalesced forming agglomerates of the irregularly shaped particles. Starting with
184 the TiO$_2$_400 sample, the particles became facetted. According to SAED data, the crystallinity
185 increased: TiO$_2$_ini and TiO$_2$_200 samples exhibited amorphous halos, but TiO$_2$_400 and further
186 samples demonstrated the SAEDs characteristic of poly-crystallites. After 800°C the particles lose
187 individual boundaries forming quite dense large crystalline objects.
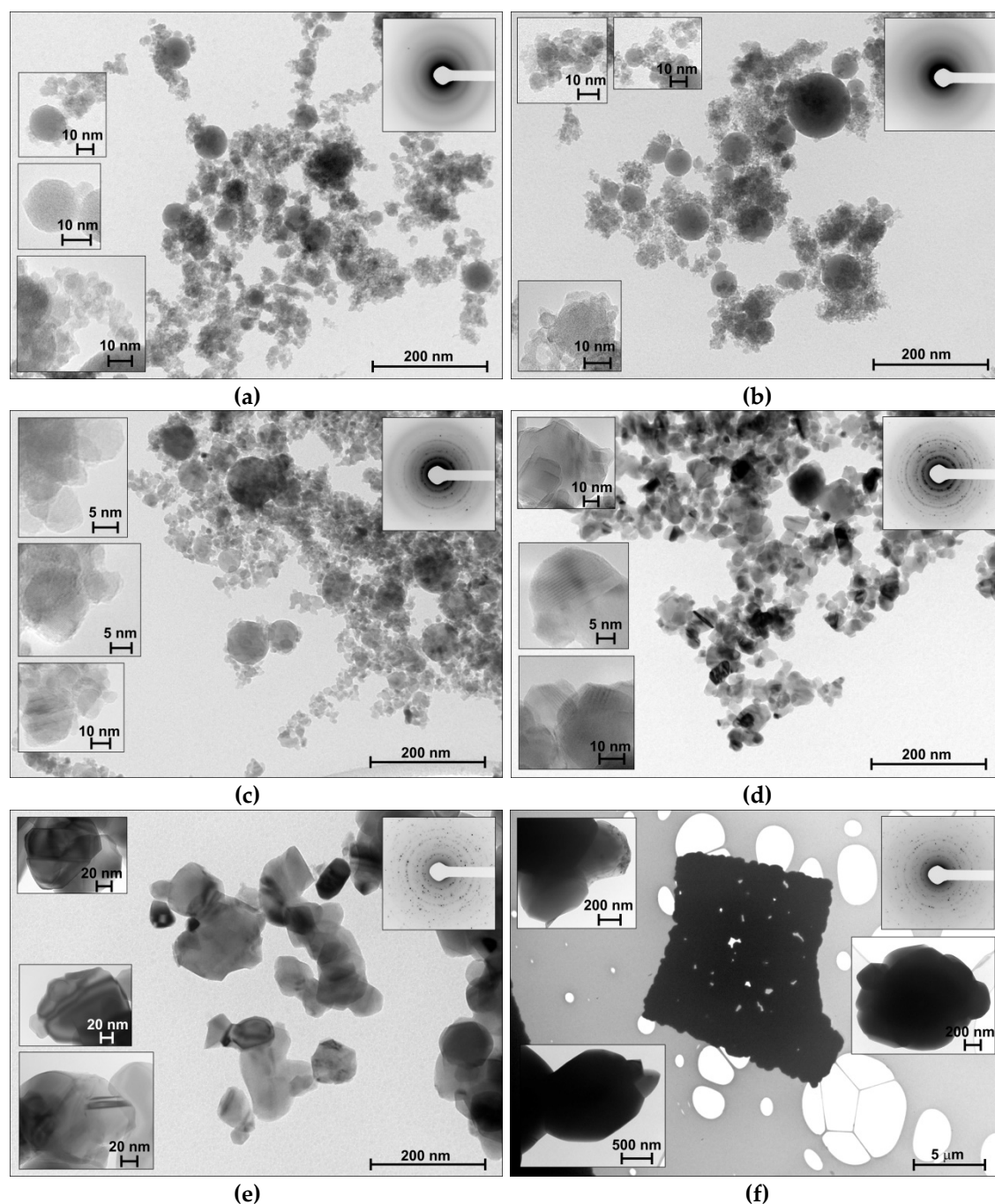
Figure 1. TEM-data for the materials: (a) TiO_2_ini, (b) TiO_2_200, (c) TiO_2_400, (d) TiO_2_600, (e) TiO_2_800, (f) TiO_2_1000. Insets: SAED data.

3.1.2. Specific surface area and porosity study

The results on the specific surface area and porosity study are presented in Figure S2 and in Table 1. Notice that the isotherms for the initial sample and the materials after thermal treatment up to 600°C are of the same type. That is these samples demonstrate a similar porous structure. Since the pores in the samples are formed by the voids between particles, the total porosity is directly depended on the size and shape of the particles. Hysteresis loop at the lower pressure (from 0.50 to 0.99) points at the mesoporous structure of the samples TiO_2_ini, TiO_2_200, TiO_2_400 and TiO_2_600. The pore size distribution for them is relatively narrow. The initial titania sample exhibits one pronounced peak in the size distribution curve. It is located at 7.5 nm and is shifted while the temperature of the thermal treatment increases. Also, its shape becomes less pronounced, which indicates that the pore size distribution widened. The sample TiO_2_800 shows the matching of the

adsorption and the desorption isotherms, which indicates the pores absence in the sample. And, these isotherms could not be registered for the TiO₂_1000 sample.

Specific surface area and pore volume values were calculated from the desorption isotherms obtained. The results are presented in Table 1. The initial sample demonstrates the largest S_{BET} of 227 m²/g. This value smoothly decreases with the increase of heating temperature до 600ºC. Further temperature increase leads to a sharp decline of the specific surface area and porosity. These results are in a good agreement with the TEM data.

Thus, the materials obtained are represented by the spherical amorphous particles growing under thermal treatment increasing crystallinity and decreasing the specific surface area and pore volume of the samples.

**Table 1.** NPs size, BET and XRD data for the samples.

Sample	Average size(nm) from TEM data	S_{BET} (m²/g)	V_{pore} (cm³/g)	Phase composition (%)		$\Delta d/d \times 10^{-3}$
				anatase	rutile	
TiO₂_ini	10	227	0.41	–	–	–
TiO₂_200	14	124	0.37	–	–	–
TiO₂_400	16	86	0.37	67	33	1.5
TiO₂_600	34	50	0.28	62	38	1.1
TiO₂_800	77	7	0.06	3	97	0.2
TiO₂_1000	400	>1	–	–	100	–

3.2. Composition study

3.2.1. X-ray diffraction data

The phase composition of the materials obtained was studied by the X-ray diffraction method. XRD patterns of the samples are presented in Figure 2. The initial material is found to be amorphous, which is consistent with the SAED data mentioned above. After 200°C treatment, the first inclusions of the anatase and rutile crystal phases can be observed, even though the sample is still amorphous. After heating at 400 and 600°C the amorphous part of the samples disappeared completely, and the anatase became the major phase (Table 2). Further temperature increase leads to the anatase-to-rutile transition.
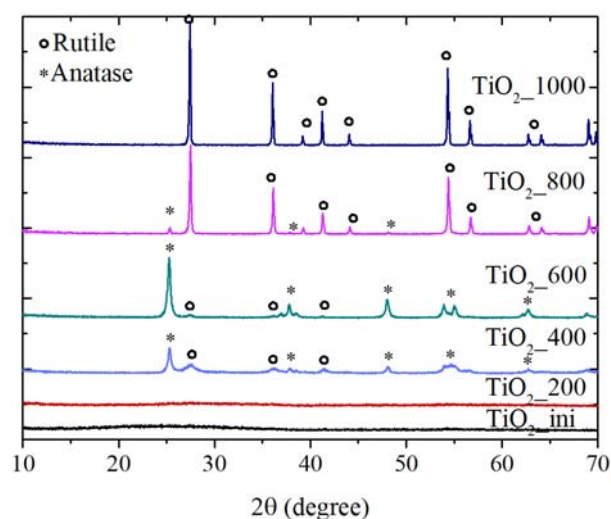

Figure 2. XRD patterns of the samples.

According to the literature, the anatase/rutile phase transition of a bulk material starts at 450°C, and at 750°C the pure rutile phase is formed [49]. In the case under study, the anatase/rutile transition takes place at a higher temperature. So, the materials obtained are characterized by the enhanced stability to the thermal-induced phase transition. This may be explained by the defects in

227 the surficial and sub-surficial layers that were formed as a result of the fast cooling of the substance
228 during the LAL process. These defects also, likely, act as a hindrance to the fast sintering of the
229 particles, which significantly appears only at 800°C (see the TEM data, section 3.1.1., and Table 1).
230   Thus, the nanoparticles obtained via LAL are amorphous. They crystallize during the thermal
231 treatment, and anatase-to-rutile transition occurs at the higher temperature pointing at the higher
232 phase stability of the material. To shed some light on the state and the crystallization process of the
233 initial material, the TG/DSC and Raman studies were performed.

234 3.2.2. TG/DSC study

235   Results of TG/DSC analysis of the initial LAL-obtained sample are presented in Figure 3. Two
236 different processes are seen at the DSC curve. The endo-thermal process at the temperatures of
237 40-200°C and the mass loss on the TG curve are associated with the removal of physically adsorbed
238 and chemically bound water. A further slight decrease in mass till 400°C is probably due to the
239 removal of carbonates from the surface of the particles. The exothermic effect on the DSC curve in
240 the temperature range of 250–450°C correlates with the crystallization of initially amorphous TiO_2.
241 At the temperatures above 600°C, the structural transformation of rutile to anatase begins, which
242 refers to the endo-thermal process.
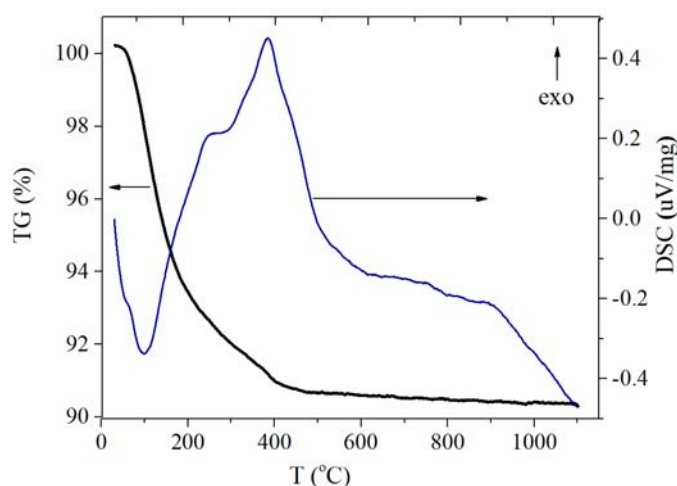
243
244 **Figure 3.** TG/DSC curves of TiO_2_ini.

245   The process of the transition of amorphous TiO_2 into the crystalline is normally observed at
246 350-400°C [50, 51]. We propose that such an early crystallization is connected with малым
247 размером частиц и the specificity of the amorphous material obtained under LAL. For example, the
248 surface and sub-surface defects, mentioned in the previous section, might be responsible for it. To
249 receive more information of the structure of as-obtained TiO_2_ini and TiO_2_200, Raman spectroscopy
250 was applied.
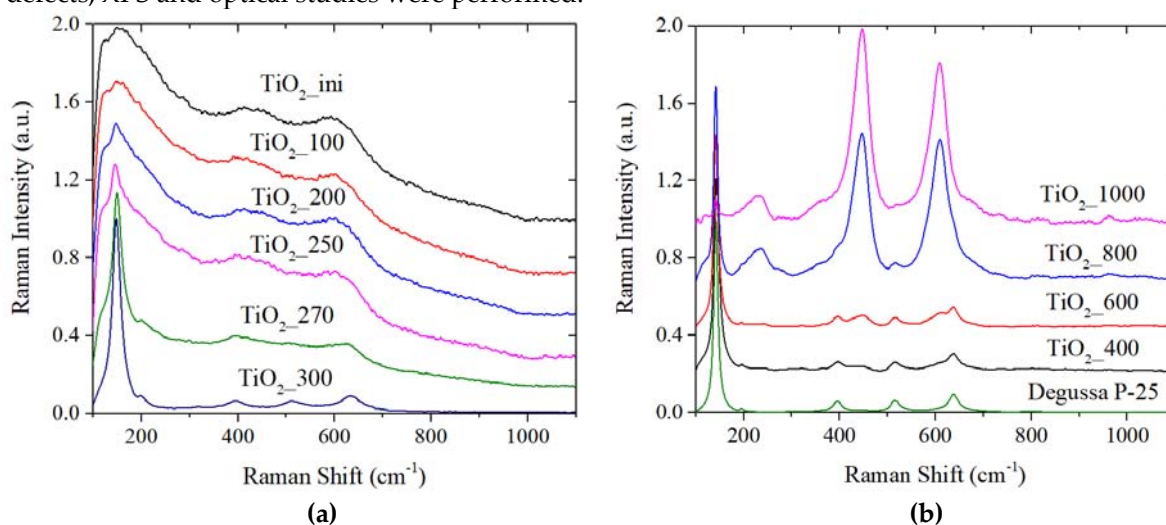
251 3.2.3. Raman spectroscopy study

252   Raman spectra of all the samples are presented in Figure 4. To study the amorphous state of the
253 initial samples, spectra for the samples after heating at 100, 250, 270 and 300°C were additionally
254 recorded. For the powders annealed up to 250°C, three wide weak bands are seen. The
255 short-wavelength band at ~150 cm^{-1} belongs to the base mode Eg for anatase. The other bands with
256 the maxima at ~420 and 600 cm^{-1} are characteristic to the rutile – Eg and A1g, respectively [52, 53].
257 Thermal treatment temperature increasing up to ~270°C leads to the pronounced anatase structure
258 forming (Figure 4a). After heating at 300°C, Raman spectra contains only anatase characteristic band
259 at 144 and 196 cm^{-1} (Eg mode), 398 cm^{-1} (B1g), 513 cm^{-1} (A1g) and 637 cm^{-1} (Eg) [52].
260   So, for the initial sample, weak bands of the rutile phase present. Characteristic anatase
261 short-wavelength band is more strong, but some inhomogeneity (appearing in different intensity

262 and wideness) can be noted. It can be proposed, that the initial sample consists of a mixture of fine
263 crystallites of anatase and rutile that have only short-range order. The thermal treatment leads to the
264 anatase crystal lattice completion, which is consistent with DSC and XRD data.

265   Further temperature increase results in the narrowing of the anatase bands (Figure 4b) that
266 indicates the particles' enlargement [54]. Then, the intensity of the rutile vibrational bands (236
267 (B1g), 446 (Eg) and 610 (A1g) cm^{-1} [55, 56]) increase. After the calcination at 800°C, rutile modes are
268 dominant in the spectra. Treatment at 1000°C results in almost complete anatase modes
269 disappearance from the spectra. This data is in good agreement with the XRD results.

270   Thus, the nanoparticles of TiO_2 obtained via LAL presumably consists of fine anatase and rutile
271 crystallites that form pure anatase and then rutile phases under thermal treatment. The material
272 shows the shift of characteristic phase-transition temperatures, which we propose is due to the
273 presence of the defects in the surficial and sub-surficial layers. To find out more information of these
274 defects, XPS and optical studies were performed.

(a)   (b)

275   **Figure 4.** Raman spectra of the samples annealed under different temperature.

276 *3.3. Surface states and functional properties study*

277 3.3.1. X-ray photoelectron spectroscopy data

278   According to the XRD, Raman, and DSC data, the initial sample undergoes structural changes
279 upon annealing to 400°C associated with the construction of the anatase crystal structure from the
280 X-ray amorphous particles. It is of interest to establish the state of titanium and surface defects
281 associated with oxygen vacancies during annealing in this temperature range. The O 1s/Ti 2p ratio
282 for the materials is presented in Table 2. The higher the temperature, the lower the ratio. This is
283 connected to the OH-groups of the adsorbed water remove from the surface that is consistent with
284 the DSC data (section 3.2.2.).

285   **Table2.** Data from the XPS spectra.

Sample	Carbon content (%)	O 1s/Ti 2p ratio
TiO_2_ini	17.4	2.67
TiO_2_200	17.2	2.58
TiO_2_400	14.4	2.44

286   The Ti 2p spectra (Figure 5a) contains only a doublet with the binding energy of 458.5 eV
287 (Ti 2p3/2) belonging to the Ti^{4+} state. Other possible titanium states (Ti^{3+}, Ti^{2+}) were not detected.
288 Thus, it can be concluded that the titanium present in the materials as titania. Photoemission spectra
289 of O 1s level are presented in Figure 5b. Deconvolution results in two peaks with the binding

energies of 529.7-530.2 and 531.9 eV. The first of them belongs to the TiO_2 lattice oxygen, and the second is for the oxygen adsorbed on the titania surface.

In addition to titanium and oxygen, carbon is present on the surface. Its amount decreases with increasing of the annealing temperature (Table 2). This is consistent with the mass loss in TG/DSC data in the range of 200-400°C. The presence of carbon can be explained by the CO_2 sorption from the air onto highly active pure particles during drying with the formation of carbonates and bicarbonates on the surface. Similar data on the carbon presence was obtained for other oxides synthesized by LAL [57].

Thus, XPS method did not detected specific titanium states (Ti^{3+}, Ti^{2+}) at the surface of the materials obtained. Then it is proposed that the defects supposed earlier may demonstrate themselves in optical properties of the materials.
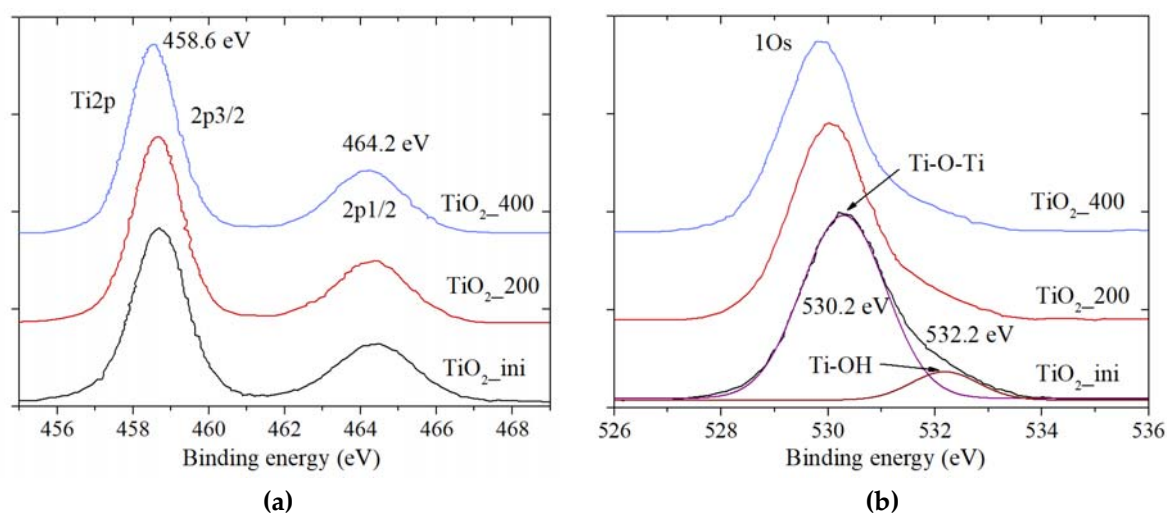

Figure 5. XPS data for the (a) Ti 2p and (b) O 1s spectra.

3.3.2. UV-visible absorption spectra

UV-Vis absorption spectra of the samples were studied by the diffusion reflectance spectra registration (Figure 6). In addition to UV absorption, all samples have additional absorption in the visible region. The initial sample exhibits the most intensive additional absorption in the long-wavelength region. This is probably due to the defective states of different nature present in the initial material. These defects amount decreases during annealing resulting in the intensity of the additional absorption decrease (curves for the TiO_2_400 and TiO_2_600 samples). However, with the further heating temperature increase to 800 and 1000°C, this additional absorption appears again. The TiO_2_800 and TiO_2_1000 samples are yellow. Normally, titania powder of any modification is white, and it turns yellow under heating turning back to white after cooling. Thus, in the case of the samples annealed at 800 and 1000°C it is proposed the possible formation of the Magneli phase [4] due to the crystal lattice restructuring with the number of oxygen atoms change. This point requires further deeper investigation.

The calculated bandgap values from DRS spectra (Figure S3) for the samples under study are presented in Table 3. It is known that bulk titania exhibits E_g of 3.2 eV for anatase and 3.0 eV for rutile. The samples obtained via LAL and annealing demonstrate decreased the E_g value. This approves the presence of energy levels of different defective states in the TiO_2 bandgap. These levels lead to the blurring of the valence and conduction bands boundary and "narrow" the bandgap.

So, the materials obtained exhibit decreased bandgap energy and defective structure that is potentially an advantage for the application in photocatalysis, etc. To reveal the nature of the defects more carefully, spectral-luminescent properties of the materials were studied.

Table 3. The band gap values for the samples determined at $[F(R)h\upsilon]^{1/2}$.

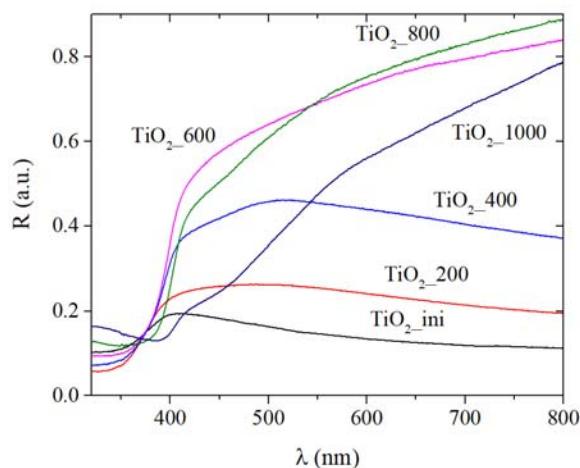| Sample	E_g, eV (Tauc)
TiO$_2$-ini	3.12
TiO$_2$-200	3.15
TiO$_2$-400	3.00
TiO$_2$-600	3.05
TiO$_2$-800	2.96
TiO$_2$-1000	2.80

Figure 6. UV-Vis spectra of titania powder.

3.3.3. Photoluminescence data

Figure 7 shows the PL spectra of all samples upon excitation either into the exciton absorption band of titanium dioxide, λ_{ex} = 300 nm (Figure 7a), or into the absorption region of defective states (Figures 6, S3), λ_{ex} = 405 nm (Figure 7b). The shape of the visible spectra upon excitation at 300 and 405 nm is similar, which indicates a significant contribution to the photoluminescence of structural defects of various natures. To analyze the defects, the published data on the luminescent properties of defects of various types was used. It is summarized in Table 4.
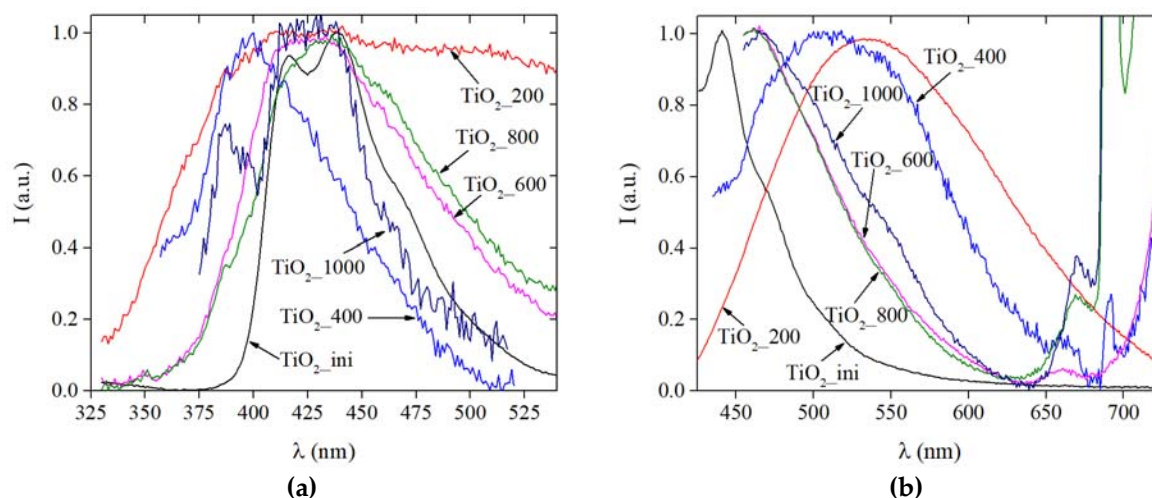

(a)

(b)

Figure 7. Photoluminescence spectra of titania powder.

The TiO$_2$_ini sample has a relatively narrow PL spectrum in the region of 300-500 nm. The most intense band with a maximum at 440 nm can be attributed to excitons localized on TiO$_6$ octahedra (the so-called self-trapped excitons, STE) [58–64]. STE states appear when an electron traps a hole in a lattice site. It is believed that STE states are localized around oxygen vacancies; therefore, they are in the band gap, but close to the valence band of titanium dioxide [61]. The shoulder at 470 nm can be attributed to oxygen vacancies of various types, the so-called F and F^{2+} centers [58-60, 64-66].

For the TiO$_2$_200 sample, the PL spectrum becomes much wider (400–700 nm). In the spectrum, STE states can be distinguished in the region of 400–450 nm. (To confirm the presence of STE states in this sample, we performed a detailed PL experiment with a sequential excitation by different wavelengths (Figure S4)). Intense bands in the 450–620 nm region relate to oxygen vacancies of various types (F, F$^+$ and F^{2+} centers): F and F^{2+} centers appear in the region of 460–470 nm, F$^+$ centers are at 520–540 nm [58-60, 64-66]. Luminescence in the range of 480–495 can also be attributed to charge transfer from Ti^{3+}, or to the oxygen anion in the octahedron [60, 61, 64], or to the sub-surface

344 oxygen vacancy [67]. Luminescence with the wavelength longer than 600 nm can be associated with
345 electronic transitions involving Ti^{3+} ions located in different positions of the crystal lattice (sites,
346 internodes), and with various types of oxygen vacancies [65]. Or it might belong to the intervalent
347 charge transfer between Ti^{3+}/Ti^{4+}, through which the electron is distributed between cations on
348 adjacent interstitial and octahedral positions [65, 68].

349 **Table 4.** PL spectra bands interpretation.

PL band	Spectral range (nm)
STE	400-450 (3.09- 2.75 eV) Y. Lei 2001 [58]; 537 (2.3 eV) 431 (2.88 eV) B. Choudhury 2014 [59]; 429 (2.89 eV) B. Choudhury 2013 [60]; 430 (2.88 eV) C. P. Saini 2017 [61]; 400-450 (3.09- 2.75 eV) M. V. Dozzi 2017 [62]; 416 (2.97 eV) W-Yu. Wu 2009 [63]; 425 (2.9 eV) S. Paul 2014 [64]
F or F^{2+}-center	420-450 (2.95-2.55 eV) V.N. Kuznetsov 2009[65]; 468 (2.65 eV) B. Choudhury 2014 [59]; 485 (2.71 eV) B. Choudhury 2013 [60]; 465 (2.67 eV) Y. Lei 2001 [58]; , 440-456 (2.81-2.71); 471 (2.63 eV) H. Zhang 2014 [66]; 457 (2.71 eV) S. Paul 2014 [64]
F^+-center	540-619 (2.30-2.00 eV) V.N. Kuznetsov 2009[64]; 525 (2.36 eV); 500 (2.48 eV) B. Choudhury 2014 [59]; , 525 (2.36 eV) Y. Lei 2001 [58]; 531(eV) H. Zhang 2014 [66]; 537 (eV) S. Paul 2014 [64]
Ti^{3+}	485 (2.55 eV) C. P. Saini 2017 [61]; 490 (2.53 eV) S. Paul 2014[64]; 480 (2.58 eV) J. Liu 2008 [67]; 491 (2.52 eV) B. Choudhury 2013 [60]

350 The TiO_2_400 sample, at the excitation in the defects region (Figure 7b) also has a wide
351 luminescence profile. However, the bands related to STE states (450 nm) are more pronounced in the
352 spectrum, and a luminescence band longer than 650 nm begins to appear.
353 The samples annealed at 600, 800, and 1000 ° C are also characterized by PL in the region of 465–
354 470 nm and intense luminescence longer than 650 nm. The intensity of the long-wavelength PL
355 increases with the increasing of the annealing temperature. A decrease in the intensity of the bands
356 in the region of 550–620 nm probably indicates a significant decrease of the amount of the F^+ centers.
357 The appearance of intense long-wavelength luminescence correlates with the appearance of
358 long-wavelength absorption in the 400–600 nm region (Figures 6, S3).
359 Thus, the nature of defects present in the titania obtained via LAL was revealed. The majority of
360 the defects are oxygen vacancies. It also was found that under irradiation these vacancies participate
361 in the specific STE states formation. Both these types of defects affect the bandgap value and may
362 play an important role in the materials' application for photocatalysis, disinfection, etc.

363 *3.4. Potential practical applications study*

364 *3.4.1. Photocatalytic activity data*

365 One of the possible applications of the dark titania obtained via LAL is a photocatalytic
366 decomposition of organic compounds in water. The challenge is to decompose stable organic
367 molecules like phenol under visible light (e.g., sunlight simulation). So, to estimate the
368 photocatalytic potential of the materials synthesized in this work, they were tested in the process of
369 photodegradation of phenol in water under visible light. The photoactivity of the materials was
370 compared with the commercial titania (Degussa P25). The sorption of the phenol onto all the
371 samples of the titania surface was less than 1 %. Figure 8 represents the results obtained for both
372 sorption and photocatalytic experiments. It can be observed that the absorbance peak of phenol at
373 275 nm decreased gradually while new characteristic peaks appeared, which indicated the
374 generation of phenolic intermediates such as p-benzoquinone (246 nm), catechol (270 nm), and
375 hydroquinone (289 nm). This result implied that in the photocatalytic degradation process, phenol
376 was first transformed into phenolic intermediates and then decomposed to CO_2 and H_2O [69]. More
377 detailed study of the phenol photodegradation products will be performed in our further work.
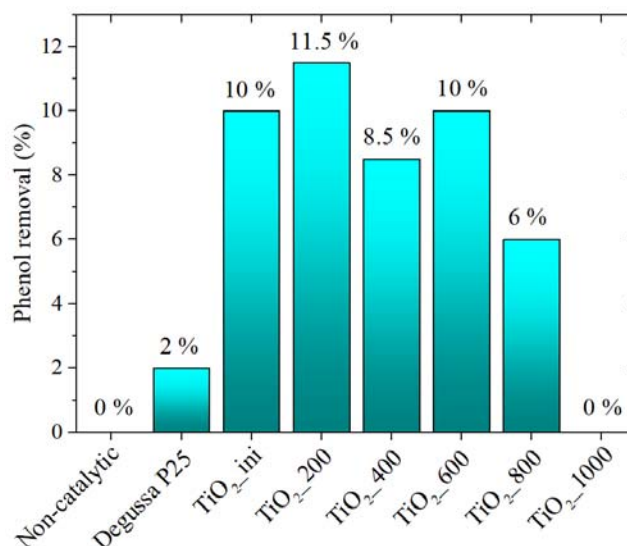
Figure 8. Photodegradation of phenol in water under visible light.

One can see that without any catalyst phenol does not decompose even under irradiation. The presence of the P25 commercial powder, this process takes place but not very intensive. Samples obtained by LAL demonstrate good catalytic activity. The TiO$_2$_200 sample seems to be the most active. This is due to the high specific surface area, the presence of absorption in the visible region (Figure 6), and the corresponding types of defects (Figure 7). Despite an increase in the rutile content and a decrease in the specific surface area, the samples remain active up to annealing temperature of 800°C. This is due to both their absorptive properties and the defective structure.

So, the materials obtained via LAL and via LAL with the following heating at 200°C exhibited photocatalytic activity in the process of phenol degradation under visible light radiation. Thus, these materials are prospective photocatalysts to investigate further.

3.4.2. Antimicrobal activity results

Titania lately is widely used as an antimicrobial agent since it is characterized by the resistance to high temperatures, low solubility, high specific surface area and strong oxidizing properties. So, the materials obtained in this work were (TiO$_2$_ini) tested in the antibacterial activity study. TiO$_2$_ini хорошо пропитывает хлопчатобумажной ткани (Figure S5). Table 7 represents the results obtained for the test of the cotton fabric covered with the TiO$_2$ particles of the various titania content against gram-positive staphylococcus (*S. aureus*) and gram-negative coli bacillus (*E. coli*).

Table 7. Antibacterial activity of dark titania towards *S. aureus* and *E. coli*.

C on tissue (mg/cm²)	The Level of Growth		Antibacterial activity A
	Control F	**Sample G**	
S.aureus (+)			
0.1	+2.8	+2.8	0
0.25	+2.8	+2.6	+0,2
1	+2.9	–2.9	+5,8
E.coli (–)			
1	+2.1	+1.0	+1,1

According to the results obtained, staphylococcus has demonstrated higher sensitivity to the TiO$_2$ presence than *E. coli* bacillus that is consistent with the literature reports [70]. The higher the titania concentration, the higher the antibacterial effect towards *S. aureus*. At the same time, the largest concentration of TiO$_2$ particles exhibited only the bacteriostatic effect on *E. coli*. This variation of the titania influence may be connected either with the different cell membranes structure of the

403 bacteria under study [71, 72] or with the contribution of the electrostatic forces between positively
404 charged cell walls of S. aureus and negatively charged centers on TiO_2 surface (oxygen vacancies).
405 However, the last point requires additional detailed investigation.
406   Thus, titania samples obtained via LAL exhibits antibacterial and bacteriostatic effects and
407 potentially may be used as a component of special bandages, antibacterial coatings, etc. It should be
408 noted that titania has an additional potential for increasing antibacterial activity [73], as well as
409 anti-cancer activity [74] by the means of photoactivation.

410 **4. Conclusions**

411   Dark titania powder was obtained via pulsed laser ablation of metallic titanium in water and
412 subsequent drying. The initial material consisting of fine anatase and rutile crystallites (5-10 nm) is
413 mesoporous with a high specific surface area (227 m^2/g). Such-prepared TiO_2 was found to be quite
414 stable under thermal treatment demonstrating the shifts of the phase transitions towards higher
415 temperatures. The material exhibited intensive visible light absorption due to additional defects'
416 levels in the band gap. For the first time for such materials, the nature of the defects was studied in
417 detail using different methods. The presence of the oxygen vacancies of three types (F, F^+, and F^{2+}
418 centers) and STE states was revealed by photoluminescence spectroscopy. It was found for the first
419 time that the irradiation of the material with the light, which wavelength energy exceeds the anatase
420 bandgap energy value, activates the STE states. The lifetime of these states is quite long and they
421 appear in the PL spectra resulting in a blue shift.
422   The changes of the dark titania powders during the thermal treatment were studied in details.
423 The materials obtained consisted of anatase or rutile, or their mixture, depending on the temperature
424 applied. The structural characteristics of the particles were changed as well, varying the heating
425 conditions. It was shown that the annealing temperature increasing led to the number of defects
426 decline, which affects the samples' color and absorption ability. The dark titania obtained via LAL
427 exhibited catalytic activity in the phenol photodegradation process under visible light and showed
428 antibacterial activity against *S. aureus* and bacteriostatic effects towards *E. coli*.

441 **References**

442 1.   Ong, C.B.; Ng, L.Y.; Mohammad A.W. A review of ZnO nanoparticles as solar photocatalysts: Synthesis,
443   mechanisms and applications. *Renewable and Sustainable Energy Reviews* **2018**, *81*, 536–551.
444 2.   Chen, X.; Mao, S.S. Titanium dioxide nanomaterials: Synthesis, properties, modifications and applications.
445   *Chem. Rev.* **2007**, *107*, 2891–2959.
446 3.   Hanaor, D.A.H.; Sorrell C.C. Review of the anatase to rutile phase transformation. *J. Mater. Sci.* **2011**, *46*,
447   855–874.
448 4.   Xu, B.; Sohn, H.Y.; Mohassab Y.; Lan, Y. Structures, preparation and applications of titanium suboxides.
449   *RSC Adv.* **2016**, *6*, 79706-79722.
450 5.   Weir, A.; Westerhoff, P.; Fabricius, L.; Hristovski, K.; von Goetz, N. Titanium dioxide nanoparticles in
451   food and personal care products. *Environ. Sci. Technol.* **2012**, *46*, 2242–2250.

6. Fujishima, A.; Rao, T.N.; Tryk, D.A. Titanium dioxide photocatalysis. *J. Photochem. Photobiol. C* **2000**, *1*, 1–21.

7. Zhang, B.; Cao, S.; Du, M.; Ye, X.; Wang, Y.; Ye, J. Titanium Dioxide (TiO₂) Mesocrystals: Synthesis, Growth Mechanisms and Photocatalytic Properties. *Catalysts* **2019**, *91*.

8. Schneider, S.L.; Lim, H.W. A review of inorganic UV filters zinc oxide and titanium dioxide. *Photodermatology Photoimmunology and Photomedicine* **2019**, *35*, 442–446.

9. Ziental, D.; Czarczynska-Goslinska, B.; Mlynarczyk, D.T.; Glowacka-Sobotta, A.; Stanisz, B.; Goslinski, T.; Sobotta, L. Titanium Dioxide Nanoparticles: Prospects and Applications in Medicine. *Nanomaterials* **2020**, *10*, 387.

10. Shabalina, A.; Fakhrutdinova, E.; Chen, Y.-W.; Lapin, I. Preparation of gold-modified F,N-TiO₂ visible light photocatalysts and their structural features comparative analysis. *J. Sol-Gel Sci. Tech.* **2015**, *75*, 617–624.

11. Liao, C.; Li, Y.; Tjong, S.C. Visible-Light Active Titanium Dioxide Nanomaterials with Bactericidal Properties. *Nanomaterials* **2020**, *10*, 124.

12. Kumaravel, V.; Mathew, S.; Bartlett, J.; Pillai, S.C. Photocatalytic hydrogen production using metal doped TiO₂: A review of recent advances. *Applied Catalysis B* **2019**, *244*, 1021–1064.

13. Chen, T.-M.; Xu, G.-Y.; Ren, H.; Zhang, H.; Tian Z.-Q.; Li J.-F. Synthesis of Au@TiO₂ core–shell nanoparticles with tunable structures for plasmon-enhanced photocatalysis. *Nanoscale Adv.* **2019**, *1*, 4522–4528.

14. Mintcheva, N.; Srinivasan, P.; Rayappan, J.B.B.; Kuchmizhak, A.A.; Gurbatov, S.; Kulinich S.A. Room-temperature gas sensing of laser-modified anatase TiO₂ decorated with Au nanoparticles. *Appl. Surf. Sci.* **2020**, *507*, 145169.

15. Mintcheva, N.; Yamaguchi, S.; Kulinich, S.A. Hybrid TiO₂-ZnO Nanomaterials Prepared Using Laser Ablation in Liquid. *Materials* **2020**, *13*, 719.

16. Yan, Y.; Yu, Y.; Wu, D.; Yang, Y.; Cao, Y. TiO₂/vanadate (Sr₁₀V₆O₂₅, Ni₃V₂O₈, Zn₂V₂O₇) heterostructured photocatalysts with enhanced photocatalytic activity for photoreduction of CO₂ into CH₄. *Nanoscale*, **2016**, *8*, 949–958.

17. Wang, M.; Nie, B.; Yee, K.-K.; Bian, H.; Lee, C.; Lee, H.K.; Zheng, B.; Lu, J.; Luo, L.; Li, Y.Y. Low-temperature fabrication of brown TiO₂ with enhanced photocatalytic activities under visible light. *Chem. Commun.*, **2016**, *52*, 2988–2991.

18. Jiang, X.; Zhang, Y.; Jiang, J.; Rong, Y.; Wang, Y.; Wu, Y.; Pan, C. Characterization of Oxygen Vacancy Associates within Hydrogenated TiO₂: A Positron Annihilation Study. *J. Phys. Chem. C* **2012**, *116*, 22619–22624.

19. Chen, X.; Liu, L.; Yu, P.Y.; Mao, S.S. Increasing Solar Absorption for Photocatalysis with Black Hydrogenated Titanium Dioxide Nanocrystals. *Science* **2011**, *331*, 746–750.

20. Ullattil, S.Gopa.; Narendranath, S.B.; Pillai, S.C.; Periyat, P. Black TiO₂ Nanomaterials: A Review of Recent Advances. *Chemical Engineering Journal* **2018**, *343*, 708–736.

21. Naldoni, A.; Allieta, M.; Santangelo, S.; Marelli, M.; Fabbri, F.; Cappelli, S.; Bianchi, C.L.; Psaro, R.; Dal Santo, V. Effect of Nature and Location of Defects on Bandgap Narrowing in Black TiO₂ Nanoparticles. *J. Am. Chem. Soc.*, **2012**, *134*, 7600–7603.

22. Han, L.; Ma, Z.; Luo, Z.; Liu, G.; Mac, J.; An, X. Enhanced visible light and photocatalytic performance of TiO₂ nanotubes by hydrogenation at lower temperature. *RSC Adv.* **2016**, *6*, 6643–6650.

23. Kang, Q.; Cao, J.; Zhang, Y.; Liu, L.; Xu H.; Ye, J. Reduced TiO₂ nanotube arrays for photoelectrochemical water splitting. *J. Mater. Chem. A* **2013**, *1*, 5766–5774.

24. Zhou H., Zhang Y. Electrochemically Self-Doped TiO₂ Nanotube Arrays for Supercapacitors. *J. Phys. Chem. C* **2014**, *118*, 5626–5636.

25. Chen, X.; Zhao, D.; Liu, K.; Wang, C.; Liu, L.; Li, B.; Zhang, Z.; Shen, D. Laser-Modified Black Titanium Oxide Nanospheres and Their Photocatalytic Activities under Visible Light. *ACS Appl. Mater. Interfaces* **2015**, *7*, 16070–16077.

26. Goncharova, D.A.; Kharlamova, T.S.; Lapin, I.N.; Svetlichnyi, V.A. Chemical and Morphological Evolution of Copper NPs Obtained by Pulsed Laser Ablation in Liquid. *J. Phys. Chem. C* **2019**, *123*, 21731–21742.

27. Zhang, D.; Zhang, C.; Liu, J.; Chen, Q.; Zhu, X.; Liang C. Carbon-Encapsulated Metal/Metal Carbide/Metal Oxide Core–Shell Nanostructures Generated by Laser Ablation of Metals in Organic Solvents. *ACS Appl. Nano Mater.* **2019**, *2*, 28–39.

28. Kanitz, A.; Kalus, M.-R.; Gurevich, E.L.; Ostendorf, A.; Barcikowski, S.; Amans, D. Review on experimental and theoretical investigations of the early stage, femtoseconds to microseconds processes during laser ablation in liquid-phase for the synthesis of colloidal nanoparticles. *Plasma Sources Sci. Technol.* **2019**, *28*, 103001.

29. Reichenberger, S.; Marzun, G.; Muhler, M.; Barcikowski, S. Perspective of Surfactant-free Colloidal Nanoparticles in Heterogeneous Catalysis. *ChemCatChem* **2019**, *11*, 1–31.

30. Kabashin, A.V.; Delaporte, P.; Pereira, A.; Grojo, D.; Torres, R.; Sarnet, T.; Sentis, M. Nanofabrication with Pulsed Lasers. *Nanoscale Res. Lett.* **2010**, *5*, 454–463.

31. Ali, N.; Bashir, S.; Umm-i-Kalsoom; Begum, N.; Rafique, M.S.; Husinsky, W. Effect of liquid environment on the titanium surface modification by laser ablation. *Appl. Surf. Sci.* **2017**, *405*, 298–307.

32. Tian, F.; Sun, J.; Yang, J.; Wu, P.; Wang, H.-L.; Du, X.-W. Preparation and photocatalytic properties of mixed-phase titania nanospheres by laser ablation, *Mater. Lett.* **2009**, *63*, 2384–2386.

33. Zimbone, M.; Buccheri, M.A.; Cacciato, G.; Sanz, R.; Rappazzo, G., Boninelli, S.; Reitano, R.; Romano, L.; Privitera, V.; Grimaldi, M.G. Photocatalytical and antibacterial activity of TiO₂ nanoparticles obtained by laser ablation in water. *Appl. Catal. B* **2015**, *165*, 487–494.

34. Sasaki, K.; Nakano, T.; Soliman, W.; Takada, N. Effect of Pressurization on the Dynamics of a Cavitation Bubble Induced by Liquid-Phase Laser Ablation. *Applied Physics Express* **2009**, *2*, 046501.

35. Jasbi, N.E.; Dorranian, D. Effect of aging on the properties of TiO₂ nanoparticle. *J. Theor. Appl. Phys.* **2016**, *10*, 157–161.

36. Huang, C.N.; Bow, J.S.; Zheng, Y.; Chen, S.Y.; Ho, N.J.; Shen, P. Nonstoichiometric Titanium Oxides via Pulsed Laser Ablation in Water. *Nanoscale Res Lett* **2010**, *5*, 972–985.

37. Semaltianos, N.G.; Logothetidis, S.; Frangis, N.; Tsiaoussis, I.; Perrie, W.; Dearden, G.; Watkins, K.G. Laser ablation in water: A route to synthesize nanoparticles of titanium monoxide. *Chem. Phys. Lett.* **2010**, *496*, 113–116.

38. De Bonis, A.; Galasso, A.; Ibris, N.; Laurita, A.; Santagata, A.; Teghil, R. Rutile microtubes assembly from nanostructures obtained by ultra-short laser ablation of titanium in liquid. *Appl. Surf. Sci.* **2013**, *268*, 571–578.

39. Amin, M.; Tomko, J.; Naddeo, J.J.; Jimenez, R.; Bubb, D.M.; Steiner, M.; Fitz-Gerald, J.; O'Malley, S.M. Laser-assisted synthesis of ultra-small anatase TiO₂ nanoparticles. *Appl. Surf. Sci.* **2015**, *348*, 30–37.

40. Guillén, G.G.; Shaji, S.; Palma, M.I.M.; Avellaneda, D.; Castillo, G.A.; Roy, T.K.D.; Gutiérrez, D.I.G.; Krishnan B. Effects of ablation energy and post-irradiation on the structure and properties of titanium dioxide nanomaterials. *Appl. Surf. Sci.* **2017**, *405*, 183–194.

41. Jafarkhani, P.; Dadras, S.; Torkamany, M.J.; Sabbaghzadeh, J. Synthesis of nanocrystalline titania in pure water by pulsed Nd:YAG laser. *Appl. Surf. Sci.* **2010**, *256*, 3817–3821.

42. Serkov, A.A.; Barmina, E.V.; Shafeev, G.A.; Voronov, V.V. Laser ablation of titanium in liquid in external electric field. *Appl. Surf. Sci.* **2015**, *348*, 16–21.

43. Hong, S.M.; Lee, S.; Jung, H.J.; Yu, Y.; Shin, J.H.; Kwon, K.Y.; Choi, M.Y. Simple Preparation of Anatase TiO₂ Nanoparticles via Pulsed Laser Ablation in Liquid. *Bull Korean Chem Soc* **2013**, *34*, 279–282

44. Amin, M.; Tomko, J.; Naddeo, J.J.; Jimenez, R.; Bubb, D.M.; Steiner, M.; Fitz-Gerald, J. O'Malley, S.M. Laser-assisted synthesis of ultra-small anatase TiO₂ nanoparticles. *Appl. Surf. Sci.* **2015**, *348*, 30–37.

45. Nath, A.; Laha, S.S.; Khare, A. Effect of focusing conditions on synthesis of titanium oxide nanoparticles via laser ablation in titanium–water interface. *Appl. Surf. Sci.* **2011**, *257*, 3118–3122.

46. Tauc, J.; Grigorovici, R.; Vancu, A. Optical Properties and Electronic Structure of Amorphous Germanium. Phys. Status Solidi 1966, 15, 627–637.

47. ISO 20743:2013. Textiles – Determination of Antibacterial Activity of Textile Products, 2nd ed.; ISO: Swizerland, 2013.

48. Gavrilenko, E.A.; Goncharova, D.A.; Lapin, I.N.; Nemoykina, A.L.; Svetlichnyi, V.A.; Aljulaih, A.A.; Mintcheva, N.; Kulinich, S.A. Comparative study of physicochemical and antibacterial properties of ZnO nanoparticles prepared by laser ablation of Zn target in water and air. *Materials* **2019**, *12*, 186.

49. Li, W.; Ni, C.; Lin, H.; Huang, C.P.; Shah, S.I. Size dependence of thermal stability of TiO₂ nanoparticles. *J. Appl. Phys.* **2004**, *96*, 6662–6668.

50. Ichinose, H.; Terasaki, M.; Katsuki, H. Synthesis of peroxo-modified anatase sol from peroxo titanic acid solution. *Journal of the Ceramic Society of Japan* **1996**, *104*, 715–718.

51. Ichinose, H.; Terasaki, M.; Katsuki, H. Properties of peroxotitanium acid solution and peroxo-modified anatase sol derived from peroxotitanium hydrate. *Journal of Sol-Gel Science and Technology* **2001**, *22*, 33–40.

52. Gotic, M.; Ivanda, M.; Popovic, S.; Music, S.; Sekulic, A.; Turkovic, A.; Furic, K. Raman investigation of nanosized TiO₂. *J. Raman Spectrosc.* **1997**, *28*, 555–558.

53. Golubovic, A.; Scepanovic, M.; Kremenovic, A.; Askrabic, S.; Berec, V.; Dohcevic-Mitrovic, Z.; Popovic, Z.V. Raman study of the variation in anatase structure of TiO₂ nanopowders due to the changes of sol–gel synthesis conditions. *J. Sol-Gel Sci. Technol.* **2009**, *49*, 311–319.

54. Gupta, S.K.; Desai, R.; Jha, P.K.; Sahoo S.; Kirin, D. Titanium dioxide synthesized using titanium chloride: size effect study using Raman spectroscopy and photoluminescence. *J. Raman Spectrosc.* **2010**, *41*, 350–355.

55. Mazza, T.; Barborini, E.; Piseri, P.; Milani, P. Raman spectroscopy characterization of TiO$_2$ rutile nanocrystals. *Phys. Rev. B* **2007**, *75*, 045416.

56. Lukacevic, I.; Gupta, S.K.; Jha, P.K.; Kirin, D. Lattice dynamics and Raman spectrum of rutile TiO$_2$: The role of soft phonon modes in pressure induced phase transition. *Mater. Chem. Phys.* **2012**, *137*, 282–289.

57. Slavinskaya, E.M.; Stadnichenko, A.I.; Muravyov, V.V.; Kardash, T.Yu.; Derevyannikova, E.A.; Zaikovskii, V.I.; Stonkus, O.A.; Lapin, I.N.; Svetlichnyi, V.A.; Boronin, A.I. Transformation of Pt-CeO$_2$ mechanical mixture of pulsed laser-ablated nanoparticles to highly active catalyst for CO oxidation. *ChemCatChem* **2018**, *10*, 2232–2247.

58. Lei, Y.; Zhang, L.D.; Meng, G.W.; Li, G.H.; Zhang, X.Y.; Liang, C.H.; Chen, W.; Wang, S.X. Preparation and photoluminescence of highly ordered TiO$_2$ nanowire arrays. *Appl. Phys. Lett.* **2001**, *78*, 1125–1127.

59. Choudhury, B.; Dey, M.; Choudhury, A. Shallow and deep trap emission and luminescence quenching of TiO$_2$ nanoparticles on Cu doping. *Appl. Nanosci.* **2014**, *4*, 499–506.

60. Choudhury, B.; Choudhury, A. Tailoring luminescence properties of TiO$_2$ nanoparticles by Mn doping *J. Luminescence* **2013**, *136*, 339–346.

61. Saini, C.P.; Barman, A.; Banerjee, D.; Grynko, O.; Prucnal, S.; Gupta, M.; Phase, D.M.; Sinha, A.K.; Kanjilal, D.; Skorupa, W.; Kanjilal, A. Impact of Self-Trapped Excitons on Blue Photoluminescence in TiO$_2$ Nanorods on Chemically Etched Si Pyramids. *J. Phys. Chem. C* **2017**, *121*, 11448−11454.

62. Dozzi, M.V.; D'Andrea, C.; Ohtani, B.; Valentini, G., Selli, E. Fluorine-Doped TiO$_2$ Materials: Photocatalytic Activity vs Time-Resolved Photoluminescence. *J. Phys. Chem. C* **2013**, *117*, 25586−25595.

63. Wu, W.-Y.; Chang, Y.-M.; Ting, J.-M. Room-Temperature Synthesis of Single-Crystalline Anatase TiO$_2$ Nanowires. *Crystal Growth & Design* **2010**, *10*, 1646−1651.

64. Paul, S.; Choudhury, A. Investigation of the optical property and photocatalytic activity of mixed phase nanocrystalline titania. *Appl. Nanosci.* **2014**, *4*, 839–847.

65. Kuznetsov, V.N.; Serpone, N.; On the Origin of the Spectral Bands in the Visible Absorption Spectra of Visible-Light-Active TiO$_2$ Specimens Analysis and Assignments. *J. Phys. Chem. C* **2009**, *113*, 15110–15123.

66. Zhang, H.; Zhou, M.; Fu, Q.; Lei, B.; Lin, W.; Guo, H.; Wu M.; Lei, Y. Observation of defect state in highly ordered titanium dioxide nanotube arrays. *Nanotechnology* **2014**, *25*, 275603.

67. Liu, J.; Li, J.; Sedhain, A.; Lin, J.; Jiang, H. Structure and Photoluminescence Study of TiO$_2$ Nanoneedle Texture along Vertically Aligned Carbon Nanofiber Arrays *J. Phys. Chem. C* **2008**, *112*, 17127–17132.

68. Khomenko, V.M.; Langer, K.; Rager, H.; Fett, A. Electronic absorption by Ti^{3+} ions and electron delocalization in synthetic blue rutile. *Phys Chem Minerals* **1998**, *25*, 338–346.

69. Wang, X.; Wang, F.; Chen, B.; Cheng, K.; Wang, J.; Zhang, J.; Song, H. Promotion of phenol photodecomposition and the corresponding decomposition mechanism over g-C$_3$N$_4$/TiO$_2$ nanocomposites *Appl. Surf. Sci.* **2018**, *453*, 320–329.

70. Varnagiris, S.; Urbonavicius, M.; Sakalauskaite, S.; Daugelavicius, R.; Pranevicius, L.; Lelis, M.; Milcius, D. Floating TiO$_2$ photocatalyst for efficient inactivation of E. coli and decomposition of methylene blue solution. *Science of the Total Environment* **2020**, *720*, 137600.

71. Romaniuk, J.A.H.; Cegelski, L. Bacterial cell wall composition and the influence of antibiotics by cell-wall and whole-cell NMR. *Philosophical Transactions of the Royal Society B* **2015**, *370*, 20150024.

72. Priyadarshini, S.; Mainal, A.; Sonsudin, F.; Yahya, R.; Alyousef, A.A.; Mohammed, A. Biosynthesis of TiO$_2$ nanoparticles and their superior antibacterial effect against human nosocomial bacterial pathogens. *Research on Chemical Intermediates*, **2020**, *46*, 1077–1089.

73. Joost, U.; Juganson, K.; Visnapuu, M.; Mortimer, M.; Kahru, A.; Nõmmiste, E.; Joost, U.; Kisand, V.; Ivask, A. Photocatalytic antibacterial activity of nano-TiO$_2$ (anatase)-based thin films: Effects on Escherichia coli cells and fatty acids. *J. Photochem. Photobiol. B* **2015**, *142*, 178–185.

74. Xu, J.; Sun, Y.; Huang, J.; Chen, C.; Liu, G.; Jiang, Y.; Zhao, Y.; Jiang, Z. Photokilling cancer cells using highly cell-specific antibody–TiO$_2$ bioconjugates and electroporation. *Bioelectrochemistry* **2007**, *71*, 217–222.